Storm-Time Thermospheric Winds Over Peru

L. A. Navarro, B. G. Fejer

Center for Atmospheric and Space Sciences, Utah State University, Logan, Utah, USA
Corresponding author: L. A. Navarro (luis.navarro.dominguez@gmail.com)

Key Points:

- Nighttime zonal disturbance winds are westward and maximum near midnight; the meridional winds are north(south)ward before(after) midnight
- The HWM14 significantly underestimate the nighttime zonal disturbance winds
- Empirical forecast of storm-time disturbance winds for large storms can be improved using multiple long-term disturbance parameters

Abstract

We used Fabry-Perot Interferometer (FPI) observations at Jicamarca, Nasca and Arequipa, Peru from 2011 to 2017 to study the nighttime zonal and meridional disturbance winds over the Peruvian equatorial region. We derived initially the seasonal-dependent average thermospheric winds corresponding to 12 hours of continuous geomagnetically quiet conditions. These quiet-time climatological winds, which are in general agreement with results from the Horizontal Wind Model (HWM14), were then used as baselines for the calculation of the disturbance winds. Our results indicate that the nighttime zonal disturbance winds are westward with peak values near midnight and with magnitudes much larger than predicted by the Disturbance Wind Model (DWM07). The premidnight equinoctial and June solstice westward disturbance winds have comparable values and increase with local time. The postmidnight westward disturbance winds decrease toward dawn and are largest during equinox and smallest during June solstice. The meridional average disturbance winds have small values throughout the night. They are northward in the premidnight sector, and southward with larger (smaller) values during December solstice (equinox) in the postmidnight sector. We also present observations showing that during the main and recovery phases of the April 2012 and May 2016 geomagnetic storms the zonal disturbance winds have much larger magnitudes and lifetimes (up to about 48 hours) than suggested by the HWM14. These observations highlight the importance of longer-term disturbance wind effects. The large and short-lived (about 2 hours) observed meridional wind disturbances are not reproduced by current climatological empirical models.

1 Introduction

Thermospheric winds are intrinsically important upper atmospheric parameters. Their transport of plasma along the geomagnetic field lines affect the chemical composition of the Earth's upper atmosphere, and are key drivers of ionospheric electric fields. Quiet-time thermospheric winds are driven mainly by horizontal pressure gradients of the diurnal atmospheric bulge caused by the solar atmospheric heating (e.g., Rishbeth, 1972; Richmond, 2011). The equatorial nighttime thermospheric zonal winds are closely coupled to the zonal drifts of the ambient plasma and of the equatorial plasma bubbles (e.g., Valladares et al., 1996; Martinis et al., 2003; Chapagain et al., 2013).

Several space-based and ground-based optical interferometers have extensively been used to monitor the dynamics of the neutral thermosphere. Fabry-Perot Interferometer observations at Arequipa, Peru (16°28’ S, 71°30’ W, dip latitude ~4° S) determined the local time, seasonal and solar flux dependence of the nighttime equatorial thermospheric winds during geomagnetically quiet periods (e.g., Meriwether et al., 1986; Biondi et al., 1990, 1991, 1999). These observations showed that solar EUV radiation driven pressure gradients control the temporal and seasonal variations of the equatorial thermospheric winds. Recently, FPI thermospheric winds measurements have also been made in the Brazilian and African equatorial regions (Meriwether et al., 2011, 2016; Makela et al., 2013; Fisher et al., 2015; Tesema et al., 2017).

Geomagnetically disturbed conditions lead to large departures of the dynamics of the thermosphere from its quiet-time pattern. Richmond and Matsushita (1975) first pointed out that geomagnetic storms generate large global equatorward propagating wind perturbations extending down to equatorial latitudes. Richmond (1978) and Richmond (1979a, 1979b) showed that Joule heating is the dominant process driving global thermospheric changes capable of reaching low latitudes. The storm-time wind circulation drives ionospheric disturbance dynamo electric fields and currents (Blanc & Richmond, 1980) that can strongly affect the middle and low latitude plasma motion and density, and the occurrence of equatorial spread F (Fejer et al., 1999). National Center for Atmospheric Research Thermosphere Ionosphere Electrodynamics General Circulation Model (NCAR/TIEGCM) simulations suggest that storm driven winds can have lifetimes of up to about 8 days at equatorial regions (Huang et al., 2005).

Several studies investigated the dynamics of the middle and low latitude geomagnetic activity driven disturbance winds using Upper Atmosphere Research Satellite (UARS) Wind Imaging Interferometer (WINDII) measurements (e.g., Fejer et al., 2000; Emmert et al 2001, 2002, 2004). These studies showed that low latitude and equatorial nighttime zonal disturbance winds are westward with peak values around 03 magnetic local time, and have small seasonal dependence. Emmert et al. (2008) used extensive satellite and ground-based wind measurements to derive the global empirical climatological Disturbance Wind Model (DWM07). In a companion paper, Drob et al. (2008) presented the Horizontal Wind Model07 (HWM07), which has both a quiet-time global wind model for the background state and the DWM07. The HWM07 provides spatial, temporal and geomagnetic activity (Ap) dependent thermospheric wind predictions. More recently, Drob et al. (2015) presented the HWM14, which consists of an updated quiet-time wind component and the DWM07. The combined HWM14 model also provides height, local time and latitude dependent predictions of the thermospheric winds as a function of the local Ap index.

Challenging Minisatellite Payload (CHAMP) satellite observations indicate that longitudinal averaged equatorial zonal disturbance winds are westward with small values during the day, and are largest near midnight, except during June solstice when they are largest around 03 LT (Xiong et al., 2015). These disturbances occur about 3-4 hours after the magnetospheric disturbances and last about 24 hours or longer, which is consistent with model results presented by Richmond and Matsushita (1975) and Blanc and Richmond (1980). CHAMP and Republic of China Satellite-1 (ROCSAT-1) satellite observations presented by Xiong et al. (2016) suggested that prompt penetration electric fields, due to sudden changes in the magnetospheric convection (e.g., Fejer, 2011), produce additional zonal disturbance winds that are westward in the afternoon sector and eastward in the post-midnight sector.

So far, few studies have examined the response of low latitude thermospheric winds to large geomagnetic storms. Emery et al. (1999) studied the thermospheric response to the November 1993 storm using TIEGCM along with the Assimilative Mapping of Ionospheric Electrodynamics (AMIE) procedure, which included data of 154 ground magnetometers and ion drift and electron precipitation measurements. These simulations showed traveling atmospheric disturbances reaching equatorial latitudes about 4 hours after the large high latitude energy depositions, and largest equatorial westward disturbances around 22 LT for all longitudes.

WINDII observations during the recovery phase of the October 1998 storm showed large latitudinal variability on the daytime disturbance winds, which reversed from westward to eastward at magnetic latitudes of about 30°, and largest disturbance winds at F-region heights (Fejer & Emmert, 2003). FPI observations from Arequipa showed reductions in the nighttime eastward and poleward winds 24 hours after the onsets of the August 1998 and October 2000 geomagnetic storms (Meriwether et al., 2013). Most recently, Malki et al. (2018) reported strong zonal and meridional thermospheric winds perturbations in the westward and equatorward directions around midnight over the northern African sector (31.2°S, 7.8°W, magnetic latitude ~23°N) 6 hours after the onset of the 27-28 February 2014 storm. These results are consistent with predicted delays in the establishment of a steady storm-driven circulation pattern (e.g., Richmond & Matsushita, 1975; Blanc & Richmond 1980).

We used extensive observations from recently deployed FPIs in the Peruvian equatorial region sector to examine for the first time the local time and seasonal dependence of the nighttime disturbance winds. In the following sections, we will first describe our database and determine our quiet-time baselines used to calculate the disturbance winds. Then, these baseline winds are compared with the corresponding quiet-time winds from HWM14. Next, we present our season-dependent disturbance wind patterns and compare them with results from the DWM07, which has been extensively used in storm-time wind studies (e.g., Malki et al., 2018). We also examine the dependence of the zonal disturbance winds on both local and extended levels of geomagnetic activity. Finally, we present measurements during and shortly after two geomagnetic storms showing that zonal disturbance winds are more accurately accounted for using multi-hour geomagnetic activity parameters (e.g., time-averaged Kp indices) than local disturbance parameters.

2 Measurement technique

Equatorial thermospheric winds are routinely monitored from FPI sites at Jicamarca (11°57’ S, 76°51’ W, dip latitude ~0°), Nasca (14°58’ S, 74°53’ W, dip latitude ~2.5° S) and Arequipa (16°28’ S, 71°30’ W, dip latitude ~4° S), since 2009, 2011 and 1984, respectively. These probes measure the 630 nm airglow Doppler-shifted emission line along specific line-of-sight directions. Starting in 2011, the FPI pointing directions have generally been cycled to provide the best sampling of the surrounding area in the central region of Peru. Figure 1 shows

the locations of the FPIs and their line-of-sights. The integration time is typically about 5 min for a single direction, and the complete cycle time is about an hour. A 632.8 nm HeNe laser observation is included at the beginning of each cycle with an integration time of 30 seconds to monitor instrumental drift. The etalon clear aperture and spacer gap for both Jicamarca and Nasca FPIs are 70 mm and 1.5 cm respectively, and 100 mm and 1 cm for Arequipa FPI. The optical design of the Jicamarca and Nasca FPIs is similar to MiniME FPI in the RENOIR network (e.g., Makela et al., 2009; Meriwether et al., 2011). The Arequipa FPI was described by Meriwether et al. (2008).

The signal recorded on every pixel of the FPI image is analyzed as the exposure of a Gaussian airglow source to the instrument transfer or Airy function. Following Harding et al. (2014), this signal is modeled by the Fredholm integral equation of the first kind between a modified Airy function and the Gaussian spectrum of the oxygen line source. The modified Airy function includes an intensity quadratic fall off factor and is blurred by a point-spread function to account for different deviations from the ideal Airy function like the radially decreasing action of the optical transmission among other optical aberrations (e.g., Meriwether et al., 2008). Since the laser has a known spectrum, the images are used to estimate different parameters of the instrumental function such as the etalon spacer gap, reflectivity, and optical magnification constant. These laser images are useful for calibration purposes and for monitoring the drift of the instrumental parameters along the night. These parameters are later used to estimate airglow parameters such like the Doppler frequency shift and broadening. More details on this method are found in Harding et al. (2014).

The line-of-sight wind velocities were calculated using the procedure described by Makela et al. (2013) and Meriwether et al. (2016) where the laser calibration images from 21-02 LT are used to get the best zero Doppler shift reference under the assumption of zero average vertical wind. This is a less restrictive assumption than that of zero instantaneous vertical wind used in past (Harding et al., 2014). As pointed out by Harding et al. (2015), the smoothest wind field can be estimated over a regional grid from a set of line-of-sight velocities considering that each of these velocities is the projection of the thermospheric wind over that particular direction. The optimal solution of the resultant underdetermined linear system imposes minimum roughness of the wind field. The roughness metric used in this regularization is expressed in

terms of the discrete approximation of the curvature and gradient operators. This way the smoothest solution is found when the roughness is minimum (Harding et al., 2015). A minimum of 8 observations was set up to enable this process and they were linearly interpolated in time to obtain a wind map field every 15 minutes on a 11x11 grid. This estimation was performed only for the horizontal wind components. Figure 1 shows the estimated wind map field at ~23:45 LT during 16th May 2013, for an assumed emission height of 250 km, obtained from 18 line-of-sight measurements.

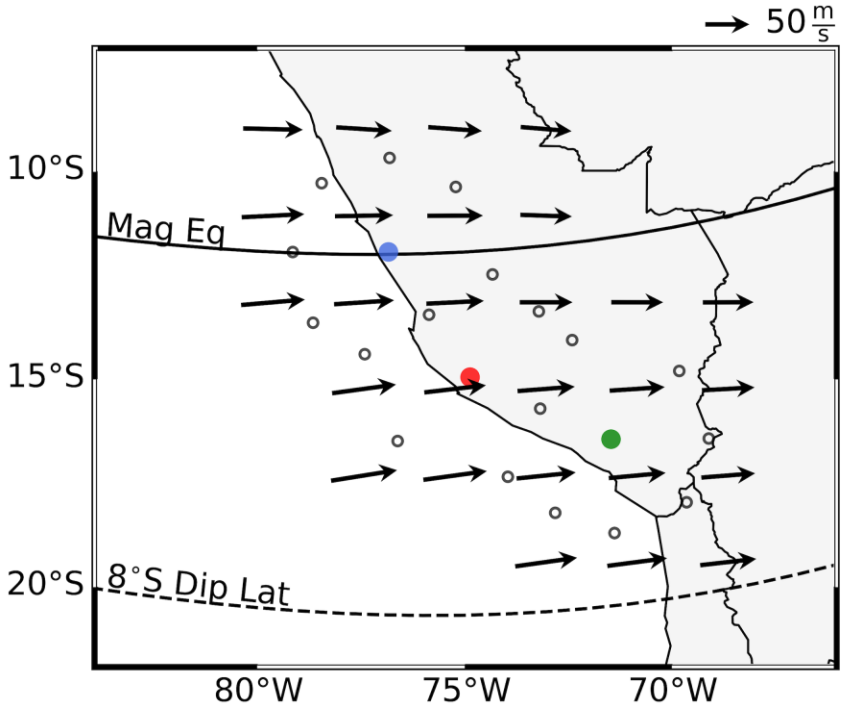

Figure 1. Estimated wind field map over central Peru for 16th May 2013 around midnight (~23:45 LT). The filled circles show the Jicamarca (blue), Nasca (red) and Arequipa (green) FPI locations; and the open circles show the sampling points for a 250 km altitude according to predetermined line-of-sight directions. Solid and dashed curves show the magnetic equator and the 8°S dip latitude, respectively.

By using the wind field estimation, we found that the zonal and meridional wind velocities over the FPI sites differed by less than about 5 m/s on average. Therefore, we combined the horizontal winds over the FPI site to improve the statistical significance of our results. The overall average thermospheric wind velocities were calculated from the estimated wind velocities over each FPI site using,

$$\bar{w} = \frac{\sum \frac{w}{\sigma^2}}{\sum \frac{1}{\sigma^2}} \quad \sigma_{\bar{w}} = \sqrt{\frac{1}{\sum \frac{1}{\sigma^2}}}$$

where w and σ are the eastward (northward) wind velocity and its corresponding estimated uncertainty over each FPI site, and $\bar{w}$ and $\sigma_{\bar{w}}$ are the average eastward (northward) wind velocity and the uncertainty of the mean velocity, respectively.

Each instrument recorded a total of ~15000 hours since 2009. However, this method requires high-quality conditions for most of the line-of-sights, and so we used 5946 hours of estimated wind fields from June 2011 to December 2017 with 15 measurements per hour on average. Since the December solstice measurements before 23 LT had generally larger errors, they were not studied. This dataset was analyzed on bimonthly bins but most of the results presented consist of 4-months seasonal averages. Table 1 shows the seasonal distribution of the number of hours available within this range. This database has the largest number of observations during June solstice and the smallest in December solstice, mostly due to the high presence of clouds during local summer. The December measurements were generally reliable only after about 23 LT.

Number of Hours	**NOV-FEB**	**MAR-APR SEP-OCT**	**MAY-AUG**
$\boldsymbol{Kp \leq 3}$	646	1930	2501
$\boldsymbol{Kp > 3}$	94	498	277

Table 1. *Seasonal Distribution of the 15-min averaged Wind Field Database.*

3 Results

3.1 Quiet-time average winds

We have derived initially bimonthly averaged geomagnetically quiet-time climatological wind patterns using various Kp-based criteria varying from local quiet ($Kp < 3-$) to very extended quiet (all $Kps < 3-$ over 48 hours) conditions. For most to the nighttime, the change in the magnitude of the zonal winds was smaller than 5 m/s. Therefore, we have chosen our reference quiet-time winds to correspond to all $Kps < 3-$ over 12 hours. In this study, our quiet-time wind patterns consist of 4-month season averages.

Figure 2 shows the seasonal dependence of our half-hour averaged quiet-time zonal and meridional winds and the corresponding results from the HWM14. The average solar flux ranged from 105 to 120 solar flux units (sfu), for equinox and June solstice and from 125 to 135 for December solstice, and the average Kp ranged from 0.7 to 1.1. The standard deviations vary from about 15 to 25 m/s for the zonal winds and from about 12 to 20 m/s for meridional winds. The HWM14 winds were first evaluated at each FPI location for an altitude of 250 km and zero geomagnetic activity level (Ap=0) every half-hour and then averaged to get an overall model prediction. The variability of the model results, calculated from the standard deviations of each half-hour bin, is shown as the shaded areas. This variability is largest during equinox and for the meridional winds.

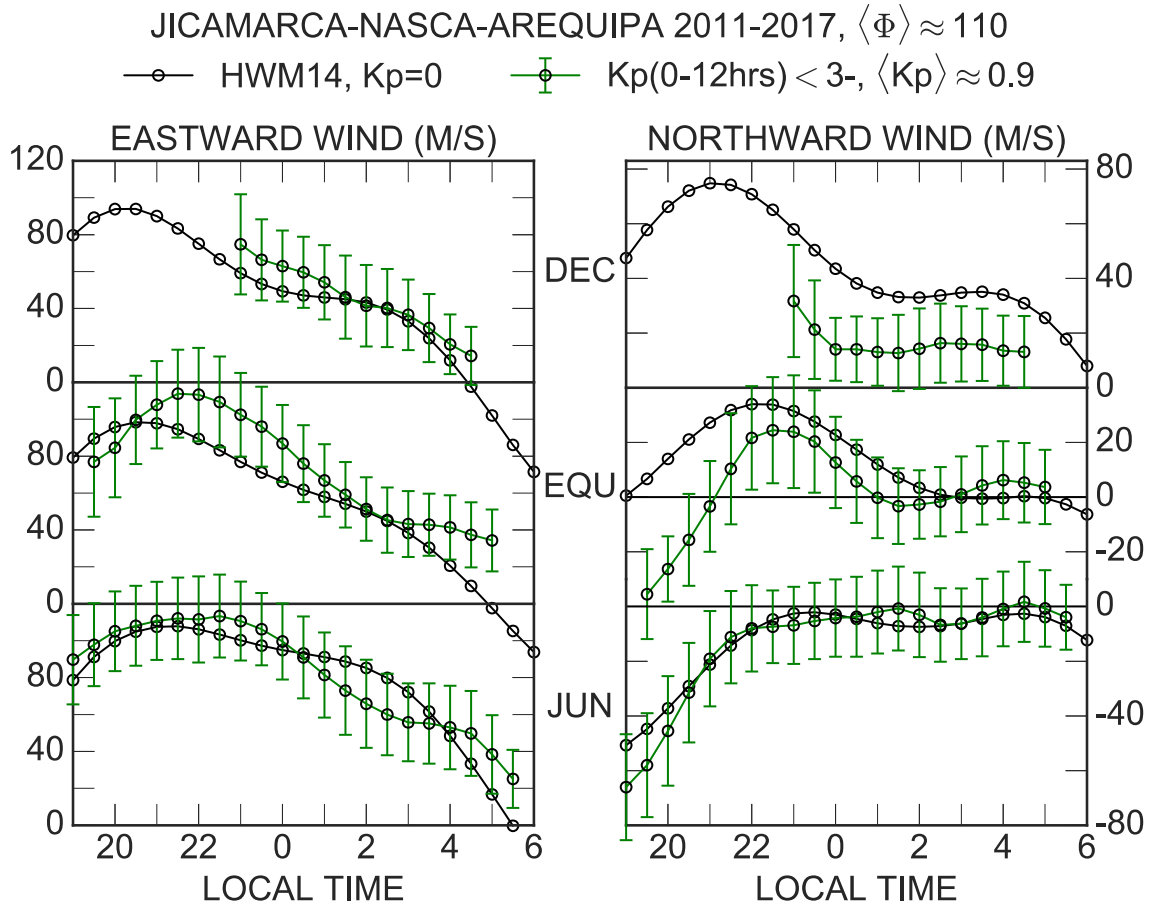

Figure 2. Seasonal variation of equatorial thermospheric winds under 12-hours of extended geomagnetic quiet conditions and the corresponding quiet-time predictions from the HWM14. The error bars and shadowed regions correspond to the standard deviations.

Figure 2 shows that for moderately low solar flux conditions our quiet-time zonal winds are eastward with peak values of about 115 m/s at about 22 LT and decrease toward dawn. The June solstice and equinoctial nighttime meridional winds are southward in the early night with decreasing magnitudes. The equinoctial meridional winds reverse to northward at about 21 LT, have a peak value of about 25 m/s near 22.5 LT, and then decrease up to about 01 LT. They have very small magnitudes in the late-night sector. The June solstice meridional winds decrease from the early night period up to about 23 LT and have small values in the postmidnight period. The December solstice meridional winds have nearly constant northward values of about 15 m/s from about midnight to 05 LT. The average wind patterns shown in Figure 2 are similar to those reported in previous equatorial studies (e.g., Biondi et al., 1990, 1999; Meriwether et al., 2016). They are also in general agreement with the predictions from the HWM14, which is expected

since a large database of Peruvian FPI measurements was used in the development of this model. However, there are also noticeable differences between the FPI and the model results. In particular, the model significantly underestimates the eastward winds in the premidnight sector and the early night southward winds during equinox, and also significantly overestimates the northward meridional wind during December solstice in the postmidnight sector, as seen from Figure 2. Some of the differences between the HWM14 and the Peruvian FPI data were already reported by Drob et al. (2015) and Meriwether et al. (2016). We will later show that the large underestimates of the quiet-time eastward winds result in significant underestimates of the disturbed zonal winds by the HWM14.

3.2 Average disturbance winds

Middle and low latitude thermospheric winds can be severely disturbed by geomagnetic storm-driven enhanced energy and momentum input into the high latitude ionosphere. Figure 3 shows the local time and seasonal dependence of our thermospheric winds for Kp>3 geomagnetic conditions, and the corresponding predictions from the HWM14. In this case, the average solar flux ranged from 105 to 125 sfu for all seasons and the average geomagnetic activity levels ranged from 3.9 to 4.3. The standard deviations shown as bars vary from 10 to 30 m/s for the zonal winds and from 12 to 25 m/s for the meridional winds. The HWM14 predictions were evaluated including its disturbance component, provided by the DWM07 (Emmert et al., 2008), at each FPI location for an altitude of 250 km, for a geomagnetic activity level of Ap=25 to correspond to the same average level of geomagnetic activity as the FPI winds (Kp≈4.1) and averaged to get the full HWM14 prediction.

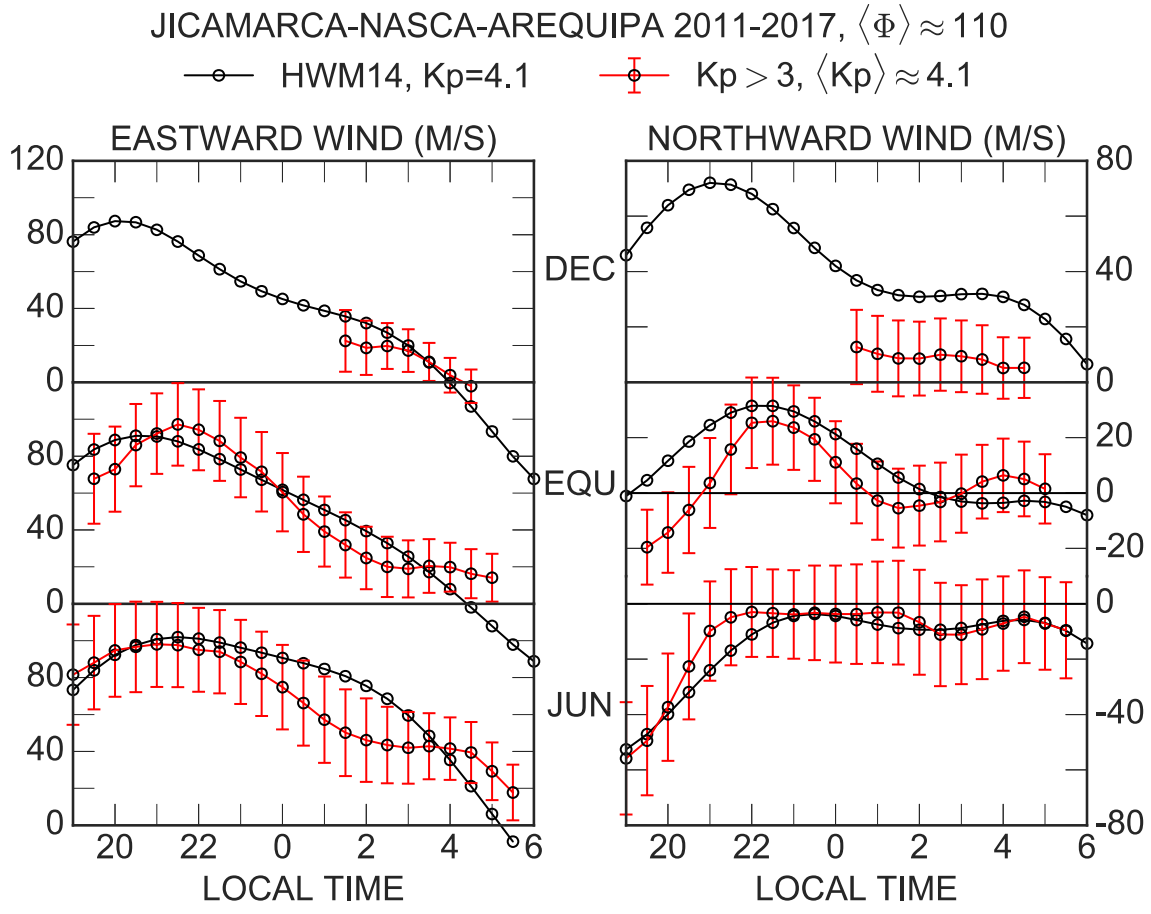

Figure 3. Seasonal comparison of disturbed equatorial thermospheric winds for local geomagnetic conditions i.e. Kp>3, and corresponding predictions from the HWM14 evaluated for Ap=25. The error bars and shadowed regions correspond to the standard deviations.

Figure 3 shows generally a much better agreement between the FPI and the HWM14 disturbed winds than between their quiet-time values. The FPI and the HWM disturbed eastward winds presented in Figure 3 are about 25 m/s and 10 m/s smaller than their corresponding quiet-time values shown in Figure 2, respectively. This difference is the result of the smaller quiet-time eastward winds predicted by the HWM14. As in the quiet-time case, the FPI and HWM meridional disturbed winds are generally in good agreement except for the equinox early night and December solstice late night periods.

Figure 4 compares our extended quiet-time seasonal patterns shown in Figure 2 and the local disturbed (Kp>3) seasonal averaged winds shown in Figure 3. As mentioned before, these patterns are half-hourly averages for the corresponding geomagnetic conditions. The standard errors of the means are about 1 m/s and 3 m/s for the extended quiet-time and local disturbed

patterns respectively. Figure 4 indicates that the average zonal disturbance winds are nearly season-independent in the premidnight sector for equinox and June solstice and largest during equinox in the postmidnight period. The meridional disturbed winds are slightly more northward in the premidnight sector for equinox and June solstice and more southward in the postmidnight sector for December and June solstices.

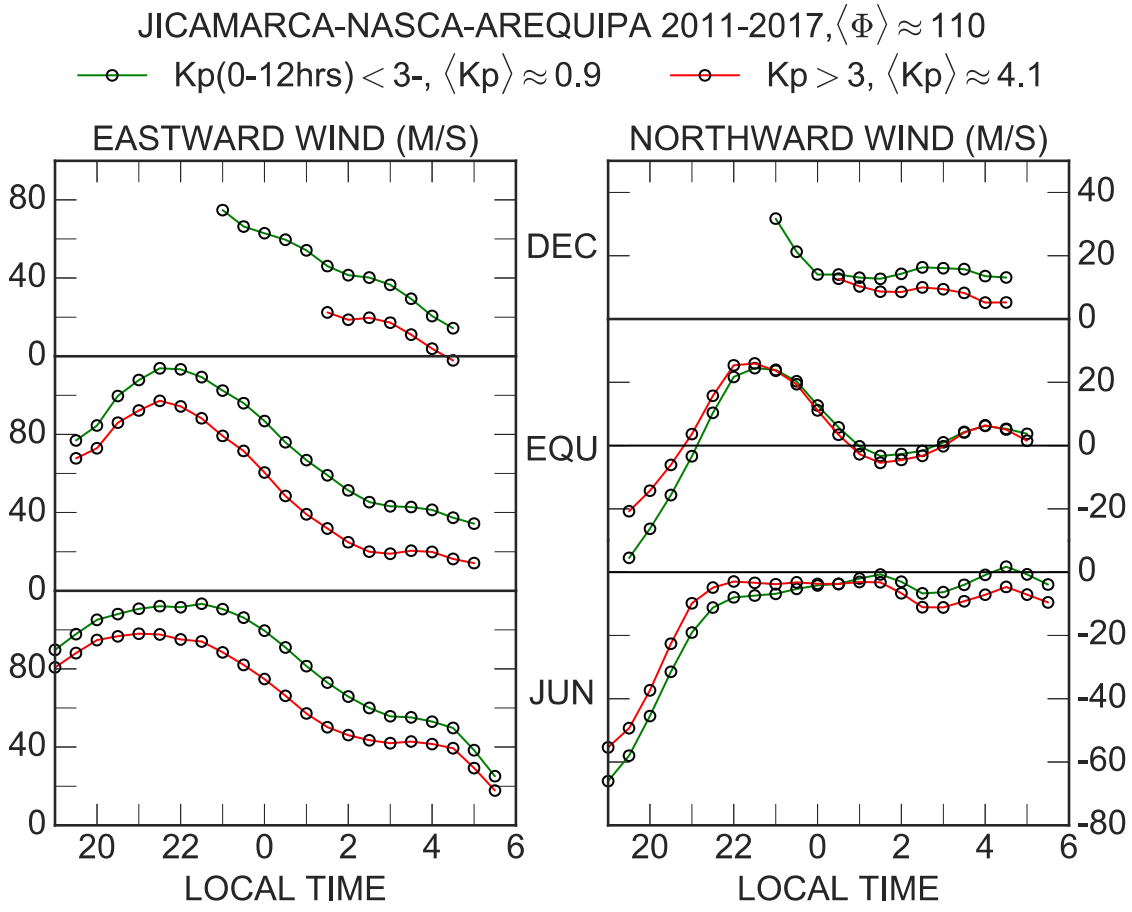

Figure 4. Comparison of 12-hours extended quiet and local disturbed thermospheric winds over Peru.

Figure 5 shows in more detail the local time and seasonal variations of the FPI disturbance winds presented in Figure 4, and the corresponding results from the seasonal-independent DWM07 (Emmert et al., 2008). The corresponding 12-hours extended quiet-time seasonal baselines were removed and the resultant disturbances were averaged in local time and season. The average geomagnetic activity enhancement, ΔKp, ranged from 3.1 to 3.3. The standard deviations are ~15 m/s most of the night, except in the early night period when they are

about 25 m/s, and the error bars indicate the standard errors of the means, which are generally about 2 m/s. The DWM07 predictions, shown as solid black lines, were evaluated at the FPI locations for an altitude of 250 km, for a geomagnetic activity level of Ap=25, which corresponds to an enhancement of ΔKp=3.2 over the geomagnetic quiet level of ⟨Kp⟩=0.9, and averaged to get a single prediction from this model.

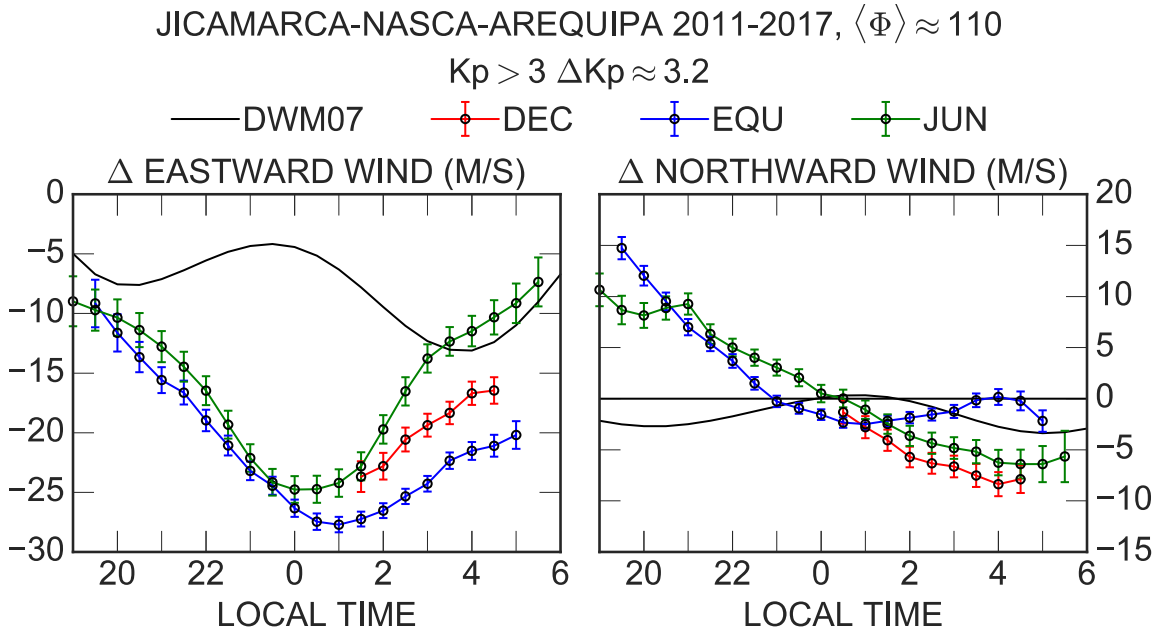

Figure 5. Local time and seasonal comparisons of FPI disturbance winds (Kp>3) with predictions from the DWM07 for geomagnetic activity enhancement of ΔKp=3.2 (Ap=25). The error bars correspond to the standard errors of the means.

Figure 5 shows that the FPI equinoctial and June solstice zonal disturbance winds have comparable values in the premidnight sector where they increase with local time and that they reach their largest magnitudes around midnight. The postmidnight zonal disturbance winds are largest (smallest) during equinox (June solstice) and decrease toward dawn at all seasons. The DWM07 predicted zonal disturbance winds have much smaller magnitudes than the FPI disturbance winds, except in the late-night period near the time of its peak value. As noted earlier, this is partly due to the HWM14 smaller quiet-time eastward winds. The meridional disturbance winds are very small at all seasons, as already shown in Figure 4. The FPI equinoctial and June solstice meridional disturbance winds are northward with comparable small values in the premidnight sector and have peak values near dusk. In the postmidnight sector, they

are southward with largest values during December solstice and smallest during equinox. The DWM07 meridional disturbance winds are southward with generally much smaller values than the FPI disturbance winds.

3.3 Extended geomagnetic activity effects

The low latitude thermosphere and ionosphere are strongly affected for periods from few hours to few days by storm-time enhanced energy deposition into the high latitude ionosphere (e.g., Blanc and Richmond, 1980; Fuller-Rowell et al., 1996). We have studied the relationships of the Peruvian FPI disturbance winds for extended periods of geomagnetic activity using up to about 12-hour averaged Kp values. The best estimates of the zonal disturbance winds were obtained using for 9-hour averaged Kp averages, but similar results were also obtained using slightly longer Kp averages. The meridional disturbances were not improved using Kp averages. Since meridional wind disturbances can have shorter lifetimes, they can be estimated best using shorter-term disturbance parameters such as hourly AE and polar cap indices. These parameters would also improve the prediction of zonal disturbance winds by taking time delay effects into account.

Figure 6 shows the equinoctial zonal disturbance winds for local and 9-hours of continuously high geomagnetic activity level. These averages were calculated following the same procedure as for the seasonal disturbances shown in Figure 5. The averages of the local and 9-hours enhanced geomagnetic activity levels ranged from 3.4 to 3.6. As expected, Figure 6 indicates that extended period of geomagnetic activity leads significant increase in the magnitude of the disturbance winds, particularly in the postmidnight period, even though the average geomagnetic activity levels are about the same. They show that for a geomagnetic activity level of Kp≈4.4 the zonal disturbance winds around midnight and in the postmidnight sector increase by ~8 m/s from local to 9-hours of steady disturbed conditions. Basically, same results were obtained for June solstice. The average meridional disturbance winds derived from local and extended disturbance conditions turned out to be essentially identical and, therefore, are not shown.

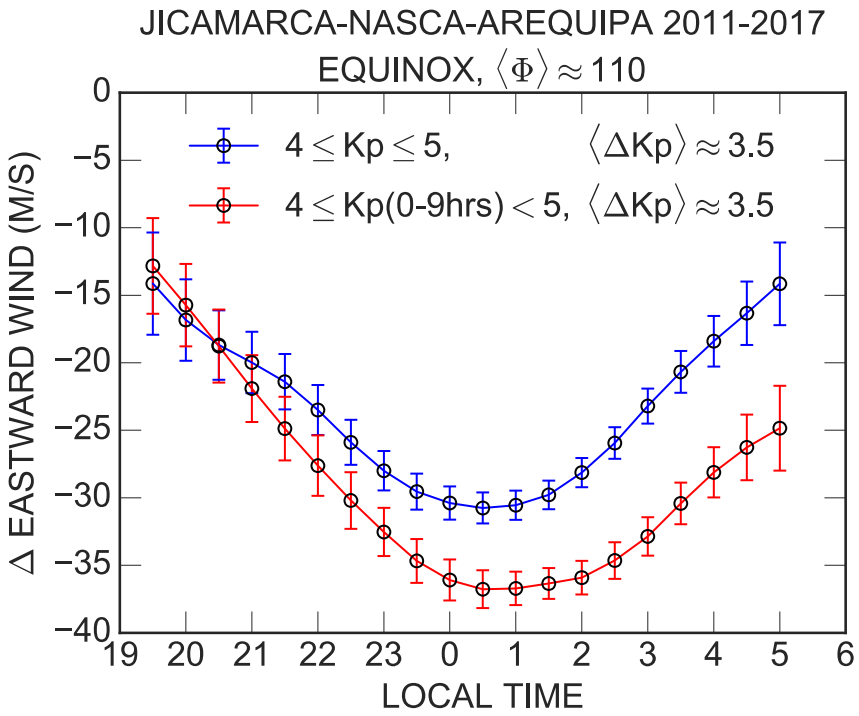

Figure 6. Comparison of equinoctial disturbance eastward winds under local and extended geomagnetically active conditions. The error bars correspond to the standard errors of the means.

We have seen that the HWM14, which includes the disturbance component from the DWM07, gives reasonably good thermospheric wind estimates over Peru during geomagnetically active times even though both its quiet and disturbance components are less accurate. We will see below that these limitations become more severe during and shortly after large geomagnetic storms when the storm time winds depend strongly also on past geomagnetic activity levels. The importance of extended periods of enhanced geomagnetic activity is also evident in storm-time equatorial plasma drifts (e.g., Scherliess & Fejer, 1997; Fejer et al., 2005). In the next section, we will compare Peruvian thermospheric measured winds during and shortly after the 23-26 April 2012 and 07-10 May 2016 long-lasting geomagnetic storms with predictions from the HWM14 and from a simple empirical disturbance model.

3.4 Case Studies

Figure 7 shows the March-June zonal disturbance winds corresponding to 9-hours of enhanced geomagnetic activity, which was determined following the procedure described earlier. This extended disturbed wind pattern is similar to that shown in Figure 6 except for the slightly

earlier time of the peak westward wind perturbation. We used this pattern to estimate the zonal wind disturbance winds for our two storms by linearly scaling their values to the corresponding local time dependent 9-hour Kp values. Therefore, our estimated zonal disturbance winds are given by

$$\mathrm{U}\left(t, \Delta\overline{\mathrm{Kp}}(0-9\ \mathrm{hrs})\right) = \mathrm{U_q}(t) + \frac{\Delta\overline{\mathrm{Kp}}(0-9\ \mathrm{hrs})}{3.1} d(t)$$

where U is the empirical zonal wind speed, t is the local time, $\mathrm{U_q}(t)$ is the corresponding 12-hour quiet-time zonal wind, $\Delta\overline{\mathrm{Kp}}(0-9\ \mathrm{hrs})$ is the average Kp enhancement over the last 9-hours over our quiet-time level (Kp=0.9), and $d(t)$ is the disturbance wind shown in Figure 7. The predicted storm-time zonal winds are obtained by adding the disturbance winds scaled from the values shown in Figure 7 to the corresponding extended quiet-time values. The storm-time meridional winds were estimated using the local Kp indices.

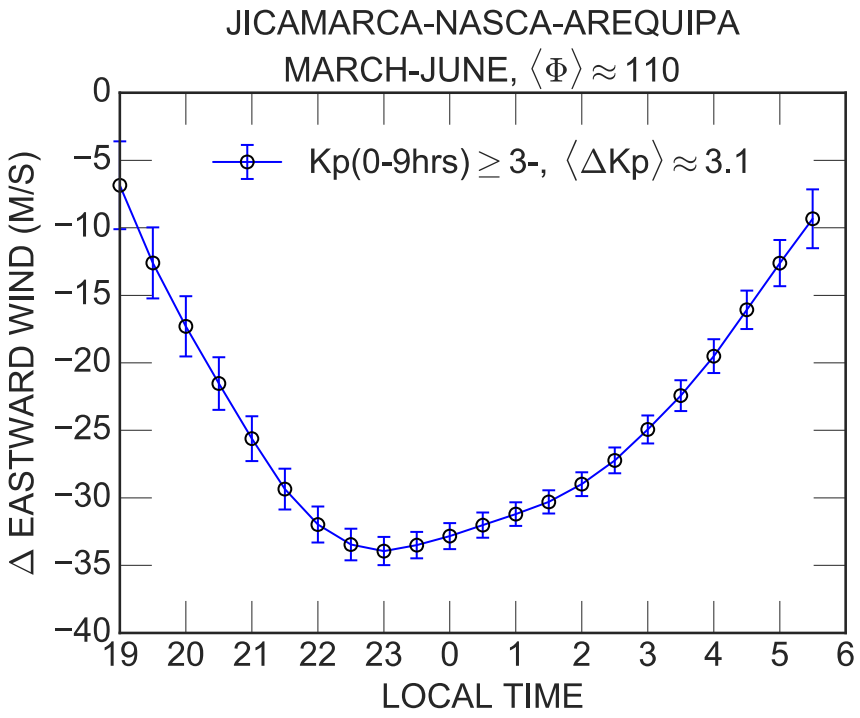

Figure 7. Disturbance eastward winds of 9-hours extended geomagnetically active conditions for the March-June period. Error bars correspond to the standard errors of the means.

Figures 8 and 9 show in the top panels the time evolution of the geomagnetic storm, as indicated by the Symmetric-H (SYMH), Auroral Electrojet (AE) and Kp indices. The bottom

panels show the zonal and meridional extended quiet-time reference winds, FPI measured zonal and meridional winds and the predictions from HWM14 and from our simple empirical model. Figure 8 shows that the main phase of the May 2016 storm lasted from ~20 LT on the 7th to ~02:30 LT on the 8th. This was followed by a highly active period of energy injections up to ~22 LT on the 8th. In this period, the AE indices reached values of ~1900 nT, and the Kp was about 6. This was followed by a long recovery phase up to about May 10th with AE values of about 500 nT, and Kp≈2.5.

Figure 8 shows that, following a relatively large short-lived northward wind disturbance at about 00:30 LT on 8 May, the zonal wind first decreased and later reversed to westward with disturbance winds of up to about 70 m/s. On the following night, the westward disturbance winds were larger than about 60 m/s from about 22 LT to 05 LT, and there was a large southward disturbance wind near midnight. The zonal disturbance winds decreased to about 50 m/s and 30 m/s in the third night and fourth nights respectively and were largely confined to the postmidnight period. The meridional winds underwent a large short-lived postmidnight northward disturbance in the third night and essentially returned to their quiet time values in the fourth night.

Figure 8 shows that the HWM14 largely underestimates the magnitudes of the westward wind perturbations in the first night, and does not account for their occurrence in the following nights. Our simple empirical model provides significantly better estimates of the westward disturbance winds, but it underestimates their peak magnitudes in the third and fourth nights. The HWM14 and our model provide nearly identical estimates of the storm-time meridional winds, which is expected, since they are both based on the local Kp values, but they do not account for the large short-lived meridional disturbances near midnight.

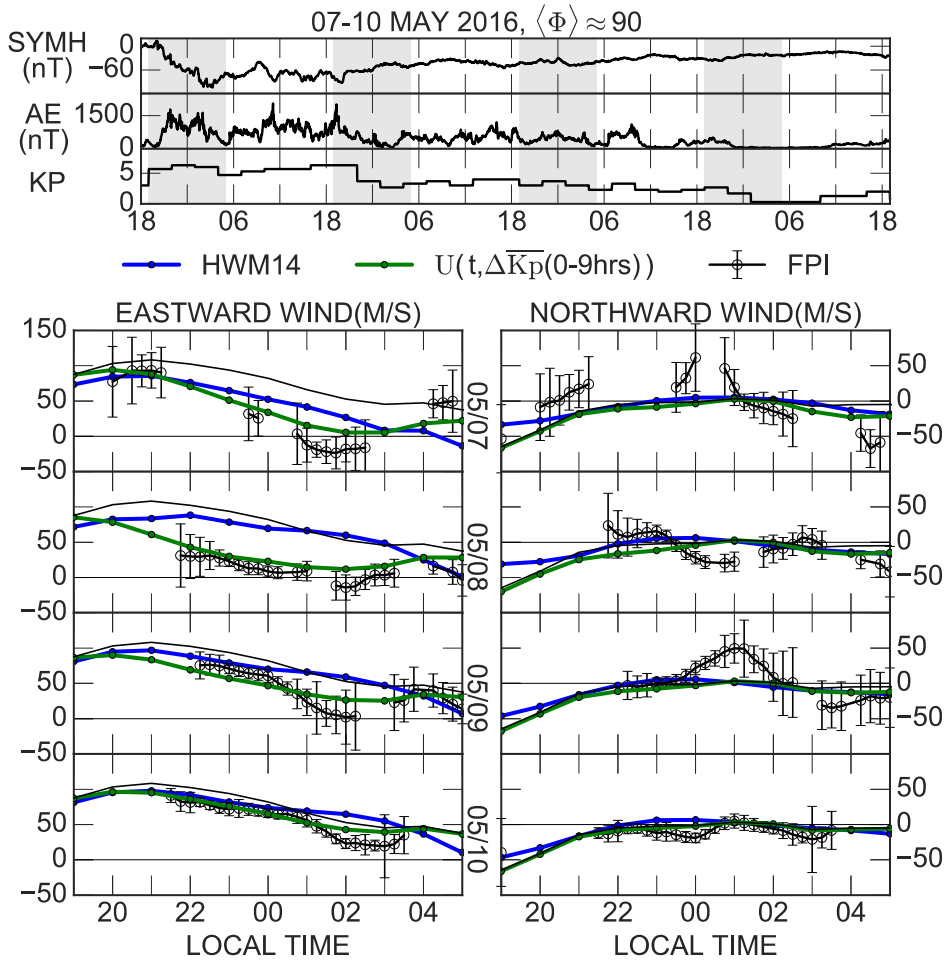

Figure 8. (Top) Geophysical indices during the main and recovery storm phases of the 07-10 May 2016 geomagnetic storm. The shadowed areas indicate night-time periods. (Bottom) Eastward and northward quiet-time reference winds (black smooth lines), FPI observations (black lines with error bars), predictions from the HWM14 (blue lines) and from our empirical model (green lines). The error bars correspond to the standard deviations of the measured winds.

Figure 9 shows the geomagnetic indices during the April 2012 geomagnetic storm and the measured and model-estimated zonal and meridional winds. The main phase of this storm occurred from ~13 LT to ~23 LT on 23 April, and its recovery phase lasted for about three days. In the main phase, the peak AE was about 1500 nT and the average Kp was close to 5+. After the main phase there was a relatively short quiet-time period followed by 2 days of moderately disturbed conditions with an average AE of about 800 nT and an average Kp of ~4.

Figure 9 shows large (peak of about 50 m/s) westward wind disturbances starting in the storm main phase and extending into the following quiet-time period. In this case, the meridional

winds underwent large northward and southward disturbances before and after midnight, respectively. In the second night, there were even larger (up to about 70 m/s) westward wind disturbances, particularly in premidnight period, while the meridional wind had northward disturbances increasing toward dawn. We note, however, that the premidnight measurements on the second night have much larger standard deviations due to less favorable observing conditions. The zonal wind disturbances decreased to about 30 m/s in the third night when they were confined to the postmidnight sector and essentially vanished in the fourth night. The meridional winds were slightly disturbed in the third night and also returned to their quiet values in the following night. The HWM14 predictions again underestimate the westward disturbances in the storm main phase, and do not account for their occurrence in the following nights. Our model reproduces the large westward disturbances in the storm main phase, but underestimates their values in the following nights, particularly in the second night. Again, these models do not reproduce the short-lived meridional wind disturbances.

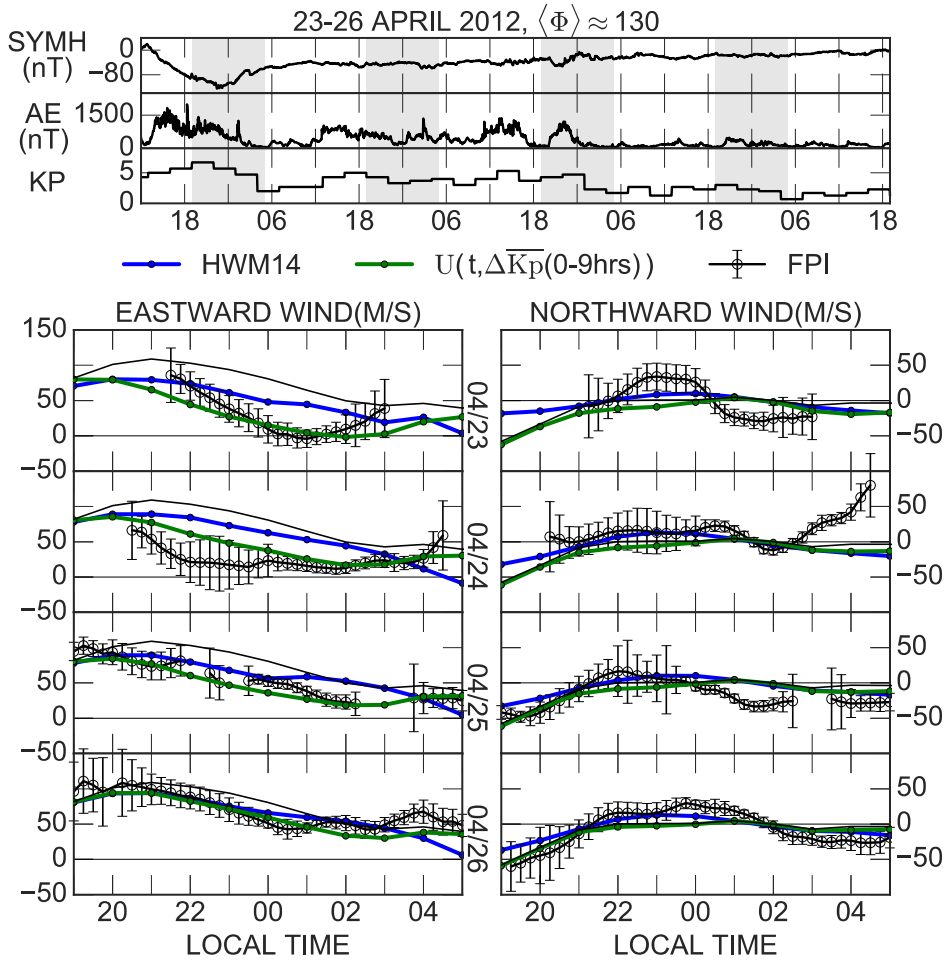

Figure 9. Same as Figure 8 for the 23-26 April 2012 geomagnetic storm.

4 Discussion

We have used multi-site FPI measurements in the Peruvian equatorial region and the novel data analysis technique presented by Harding et al. (2015) to determine for the first time the local time and seasonal dependence of the nighttime equatorial extended quiet and disturbed zonal and meridional winds, and compared them with predictions from HWM14 and DWM07. We have determined that the magnitudes of the equatorial nighttime eastward winds increase slightly from local to extended quiet conditions, and have used 12-hours extended-quiet average winds as our baseline for inferring geomagnetic activity driven disturbance winds. Our extended zonal and meridional quiet-time climatologies are in good agreement with results from previous equatorial wind studies (e.g., Biondi et al., 1990, 1999; Meriwether et al., 2016), and consistent with quiet-time F-region zonal plasma drifts (e.g., Fejer et al., 1991, 2005). They are also in general agreement with predictions from the HWM14, although this model tends to underestimate the Peruvian nighttime eastward winds.

We showed that the June solstice and equinoctial premidnight westward wind disturbances have comparable magnitudes and increase up to about midnight. Later, they decrease toward dawn and are largest during equinox and smallest during June solstice. The equinoctial and June solstice meridional disturbance winds are northward with comparable values in the premidnight sector and decrease monotonically from dusk to midnight where they reverse to southward. In the postmidnight sector, the southward disturbance winds increase toward dawn and have largest values during December solstice and smallest during equinox.

Emmert et al. (2004) presented longitudinally averaged disturbance zonal winds derived from climatological WINDII-UARS satellite measurements with peak magnitude around 03 LT, and showed that this peak moves to earlier local times with increasing geomagnetic activity. The DWM07 also predicts nighttime westward disturbance winds over Arequipa at 03 LT (Emmert et al., 2008). We note, however, that the FPI derived zonal disturbance winds over Arequipa presented in Figure 8 of the DWM07 study have larger values at midnight than at 03 LT, consistent with our data. CHAMP satellite measurements showed strongest zonal wind disturbances around midnight during equinox and December solstice, and near 03 LT during

June solstice (Xiong et al., 2015). Clearly, additional studies are needed to fully characterize the seasonal, solar cycle, and longitudinal variations of the equatorial disturbance winds.

We have seen that the DWM07 significantly underestimates, particularly near midnight, the magnitude of the nighttime zonal disturbance winds. Thermospheric wind measurements over the North African low latitude region during the 27-28 February 2014 storm showed that the DWM07 also significantly underestimated the nighttime westward disturbance winds near midnight (Malki et al., 2018). Our simple empirical model provides improved estimates of the storm-driven zonal perturbations for the two geomagnetic storms considered above. This is especially the case in the early phases of the storms. The model predictions for nights after the main phases could be improved by introducing a longer-term disturbance parameter. Fejer et al. (2005) showed that large westward postmidnight F-region disturbance dynamo drifts are also associated with time delays of about 15-24 hours after enhanced geomagnetic activity. Our database is not extensive enough for determining the possible effects of these longer-term disturbance parameters. The DWM07 and our model give reasonable estimates of the average meridional disturbance winds, but are unable to account for short-term disturbances; which are probably associated with large-scale trans-equatorial travelling atmospheric disturbances originated by energy depositions at polar regions with time delays of about 4 to 6 hours (Xiong et al., 2015; Zhang et al., 2017; Malki et al., 2018). The use of shorter-term disturbance parameters would also improve the prediction of both zonal and meridional disturbance winds by taking time delay effects into account.

5 Summary and conclusions

We have presented the first study of the local time and seasonal dependence of the nighttime equatorial disturbance winds over Peru. Thes~~e~~ disturbance winds are westward with largest magnitudes around midnight and strong seasonal dependence in the postmidnight period. The equinoctial and June solstice premidnight meridional disturbance winds are northward and have comparable magnitudes. In the postmidnight sector, they are southward with larger values during December solstice and smallest during equinox. The DWM07 significantly underestimates the magnitudes of the nighttime equatorial zonal disturbance winds over Peru, particularly close to midnight. The zonal disturbance winds cannot be accurately predicted using only local disturbance parameters such as the 3-hour Kp indices. Time extended disturbance

effects are particularly important during recovery phases of geomagnetic storms when significant postmidnight disturbance winds can last longer than 48 hours after storm main phases. The short-lived equatorial meridional disturbance winds cannot be accounted for with current empirical models.

Acknowledgments, Samples, and Data

This work was supported by the NASA H-LWS program through grant 80NSSC17K071 and by a fellowship from the Howard L. Blood Endowment. The FPI network in Peru is operated and maintained by technicians and engineers at the Jicamarca Radio Observatory with support from Clemson University and New Jersey Institute of Technology. The Jicamarca Radio Observatory is a facility of the Instituto Geofisíco del Perú operated with support from NSF award AGS-1732209 through Cornell University. The FPI data is available at the website of the Jicamarca Radio Observatory (http://jro.igp.gob.pe), and the geomagnetic indices are available from the World Data Center for Geomagnetism, Kyoto (http://wdc.kugi.kyoto-u.ac.jp) and from the National Centers for Environmental Information of the National Oceanic and Atmospheric Administration (https://www.ngdc.noaa.gov). We thank Prof. John Meriwether at Clemson University for his efforts in helping to establish the network of three Fabry-Perot interferometer observatories in Peru, to Marco Milla for useful suggestions, and to Brian Harding for providing the computational program to analyze, process and estimate the wind fields. Thanks are also due to the Jicamarca staff, to Oscar Veliz and Ricardo Rojas in particular, for support with the FPI operations.

References

Biondi, M. A., Meriwether Jr., J. W., Fejer, B. G., & Gonzalez, S. A. (1990). Seasonal variations in the equatorial thermospheric wind measured at Arequipa, Peru. *Journal of Geophysical Research: Space Physics*, 95(A8), 12243-12250. doi: 10.1029/JA095iA08p12243

Biondi, M. A., Meriwether Jr., J. W., Fejer, B. G., Gonzalez, S. A., & Hallenbeck, D. C. (1991). Equatorial thermospheric wind changes during the solar cycle: Measurements at Arequipa, Peru, from 1983 to 1990. *Journal of Geophysical Research: Space Physics*, 96(A9), 15917-15930. doi: 10.1029/91JA01645

Biondi, M. A., Sazykin, S. Y., Fejer, B. G., Meriwether, J. W., & Fesen, C. G. (1999). Equatorial and low latitude thermospheric winds: Measured quiet time variations with season and solar flux from 1980 to 1990. *Journal of Geophysical Research: Space Physics*, 104(A8), 17091-17106. doi: 10.1029/1999JA900174

Blanc, M., & Richmond, A. D. (1980). The ionospheric disturbance dynamo. *Journal of Geophysical Research: Space Physics*, 85(A4), 1669-1686. doi: 10.1029/JA085iA04p01669

Chapagain, N. P., Fisher, D. J., Meriwether, J. W., Chau, J. L., & Makela, J. J. (2013). Comparison of zonal neutral winds with equatorial plasma bubble and plasma drift velocities. *Journal of Geophysical Research: Space Physics*, 118(4), 1802-1812. doi: 10.1002/jgra.50238

Drob, D. P., Emmert, J. T., Crowley, G., Picone, J. M., Shephred, G. G., Skinner, W., Hays, P., Niciejewski, R. J., Larsen, M., She, C. Y., Meriwether, J. W., Hernandez, G., Jarvis, M. J., Sipler, D. P., Tepley, C. A., O'Brien, M. S., Bowman J. R., Wu, Q., Murayama, Y., Kawamura, S., Reid, I. M. & Vincent, R. A. (2008). An empirical model of the Earth's horizontal wind fields: HWM07. *Journal of Geophysical Research: Space Physics*, 113(A12). doi: 10.1029/2008JA013668

Drob, D. P., Emmert, J. T., Meriwether, J. W., Makela, J. J., Doornbos, E., Conde, M., Hernandez, G., Noto, J., Zawdie, K. A., McDonald, S. E., Huba, J. D. & Klenzing, J. H. (2015). An update to the Horizontal Wind Model (HWM): The quiet time thermosphere. *Earth and Space Science*, 2(7), 301-319. doi: 10.1002/2014EA000089

Emery, B., Lathuillere, C., Richards, P., Roble, R., Buonsanto, M., Knipp, D., Wilkinson, P., Sipler, D. P. & Niciejewski, R. (1999). Time dependent thermospheric neutral response tothe 2–11 November 1993 storm period. *Journal of Atmospheric and Solar-Terrestrial Physics*, 61(3), 329-350. doi: https://doi.org/10.1016/S1364-6826(98)00137-0

Emmert, J. T., Drob, D. P., Shepherd, G. G., Hernandez, G., Jarvis, M. J., Meriwether, J. W., Niciejewski, R. J., Sipler, D. P. & Tepley, C. A. (2008). DWM07 global empirical model of upper thermospheric storm-induced disturbance winds. *Journal of Geophysical Research: Space Physics*, 113(A11). doi: 10.1029/2008JA013541

Emmert, J. T., Fejer, B. G., Fesen, C. G., Shepherd, G. G., & Solheim, B. H. (2001). Climatology of middle- and low-latitude daytime F region disturbance neutral winds measured by Wind Imaging Interferometer (WINDII). *Journal of Geophysical Research: Space Physics*, 106(A11), 24701-24712. doi: 10.1029/2000JA000372

Emmert, J. T., Fejer, B. G., Shepherd, G. G., & Solheim, B. H. (2002). Altitude dependence of middle and low-latitude daytime thermospheric disturbance winds measured by WINDII. *Journal of Geophysical Research: Space Physics*, 107(A12), SIA 19-1-SIA 19-15. doi: 10.1029/2002JA009646

Emmert, J. T., Fejer, B. G., Shepherd, G. G., & Solheim, B. H. (2004). Average nighttime F region disturbance neutral winds measured by UARS WINDII: Initial results. *Geophysical Research Letters*, 31(22). doi: 10.1029/2004GL021611

Fejer, B. G. (2011). Low Latitude Ionospheric Electrodynamics. *Space Science Reviews*, 158(1), 145–166. doi: 10.1007/s11214-010-9690-7

Fejer, B. G., de Paula, E. R., González, S. A., & Woodman, R. F. (1991). Average vertical and zonal F region plasma drifts over Jicamarca. *Journal of Geophysical Research: Space Physics*, 96(A8), 13901-13906. doi: 10.1029/91JA01171

Fejer, B. G., & Emmert, J. T. (2003). Low-latitude ionospheric disturbance electric field effects during the recovery phase of the 19–21 October 1998 magnetic storm. *Journal of Geophysical Research: Space Physics*, 108(A12). doi: 10.1029/2003JA010190

Fejer, B. G., Emmert, J. T., Shepherd, G. G., & Solheim, B. H. (2000). Average daytime F region disturbance neutral winds measured by UARS: Initial results. *Geophysical Research Letters*, 27(13), 1859-1862. doi: 10.1029/2000GL003787

Fejer, B. G., Scherliess, L., & de Paula, E. R. (1999). Effects of the vertical plasma drift velocity on the generation and evolution of equatorial spread F. *Journal of Geophysical Research: Space Physics*, 104(A9), 19859-19869. doi: 10.1029/ 1999JA900271

Fejer, B. G., Souza, J. R., Santos, A. S., & Costa Pereira, A. E. (2005). Climatology of F region zonal plasma drifts over Jicamarca. *Journal of Geophysical Research: Space Physics*, 110(A12). doi: 10.1029/2005JA011324

Fisher, D. J., Makela, J. J., Meriwether, J. W., Buriti, R. A., Benkhaldoun, Z., Kaab, M., & Lagheryeb, A. (2015). Climatologies of nighttime thermospheric winds and temperatures from Fabry-Perot interferometer measure- ments: From solar minimum to solar maximum. *Journal of Geophysical Research: Space Physics*, 120(8), 6679-6693. doi: 10.1002/2015JA021170

Fuller-Rowell, T. J., Codrescu, M. V., Rishbeth, H., Moffett, R. J., & Quegan, S. (1996). On the seasonal response of the thermosphere and ionosphere to geo- magnetic storms. *Journal of Geophysical Research: Space Physics*, 101(A2), 2343-2353. doi: 10.1029/95JA01614

Harding, B. J., Gehrels, T. W., & Makela, J. J. (2014). Nonlinear regression method for estimating neutral wind and temperature from Fabry-Perot interferometer data. *Applied Optics*, 53(4), 666–673. doi: 10.1364/AO.53.000666

Harding, B. J., Makela, J. J., & Meriwether, J. W. (2015). Estimation of mesoscale thermospheric wind structure using a network of interferometers. *Journal of Geophysical Research: Space Physics*, 120(5), 3928-3940. doi: 10.1002/2015JA021025

Huang, C.-M., Richmond, A. D., & Chen, M.-Q. (2005). Theoretical effects of geomagnetic activity on low-latitude ionospheric electric fields. *Journal of Geophysical Research: Space Physics*, 110(A5). doi: 10.1029/ 2004JA010994

Makela, J. J., Fisher, D. J., Meriwether, J. W., Buriti, R. A., & Medeiros, A. F. (2013). Near-continual ground-based nighttime observations of thermospheric neutral winds and temperatures over equatorial brazil from 2009 to 2012. *Journal of Atmospheric and Solar-Terrestrial Physics*, 103, 94 - 102. doi: https://doi.org/10.1016/j.jastp.2012.11.019

Makela, J. J., Meriwether, J. W., Lima, J. P., Miller, E. S., & Armstrong, S. J. (2009). The Remote Equatorial Nighttime Observatory of Ionospheric Regions project and the International Heliospherical Year. *Earth, Moon, and Planets*, 104(1), 211–226. doi: 10.1007/s11038-008-9289-0

Malki, K., Bounhir, A., Benkhaldoun, Z., Makela, J. J., Vilmer, N., Fisher, D. J., Kaab, M., Elbouyahyaoui, K., Harding, B. J., Laghriyeb, A., Daassou, A. & Lazrek, M. (2018). Ionospheric and thermospheric response to the 27–28 February 2014 geomagnetic storm over north Africa. *Annales Geophysicae*, 36(4), 987–998. doi: 10.5194/angeo-36-987-2018

Martinis, C., Eccles, J. V., Baumgardner, J., Manzano, J., & Mendillo, M. (2003). Latitude dependence of zonal plasma drifts obtained from dual-site airglow observations. *Journal of Geophysical Research: Space Physics*, 108(A3). doi: 10.1029/2002JA009462

Meriwether, J. W., Faivre, M., Fesen, C., Sherwood, P., & Veliz, O. (2008). New results on equatorial thermospheric winds and the midnight temperature maximum. *Annales Geophysicae*, 26(3), 447–466. doi: 10.5194/angeo-26-447-2008

Meriwether, J. W., Makela, J., Fisher, D., Buriti, R., Medeiros, A., Akmaev, Fuller-Rowell, T. J. & Wu, F. (2013). Comparisons of thermospheric wind and temperature measurements in equatorial Brazil to Whole Atmosphere Model Predictions. *Journal of Atmospheric and Solar-Terrestrial Physics*, 103, 103 - 112. doi: 10.1016/j.jastp.2013.04.002

Meriwether, J. W., Makela, J. J., & Fisher, D. J. (2016). Simultaneous Measurements and Monthly Climatologies of Thermospheric Winds and Temperatures in the Peruvian and Brazilian Longitudinal Sectors. *In Ionospheric space weather* (p. 175-186). American Geophysical Union (AGU). doi: 10.1002/9781118929216.ch15

Meriwether, J. W., Makela, J. J., Huang, Y., Fisher, D. J., Buriti, R. A., Medeiros, A. F., & Takahashi, H. (2011). Climatology of the nighttime equatorial thermospheric winds and temperatures over Brazil near solar minimum. *Journal of Geophysical Research: Space Physics*, 116(A4). doi: 10.1029/2011JA016477

Meriwether, J. W., Moody, J. W., Biondi, M. A., & Roble, R. G. (1986). Optical interferometric measurements of nighttime equatorial thermospheric winds at Arequipa, Peru. *Journal of Geophysical Research: Space Physics*, 91(A5), 5557-5566. doi: 10.1029/JA091iA05p05557

Richmond, A. D. (1978). Gravity wave generation, propagation, and dissipation in the thermosphere. *Journal of Geophysical Research: Space Physics*, 83(A9), 4131-4145. doi: 10.1029/JA083iA09p04131

Richmond, A. D. (1979a). Large-amplitude gravity wave energy production and dissipation in the thermosphere. *Journal of Geophysical Research: Space Physics*, 84(A5), 1880-1890. doi: 10.1029/JA084iA05p01880

Richmond, A. D. (1979b). Thermospheric heating in a magnetic storm: Dynamic transport of energy from high to low latitudes. *Journal of Geophysical Research: Space Physics*, 84(A9), 5259-5266. doi: 10.1029/JA084iA09p05259

Richmond, A. D. (2011). Electrodynamics of Ionosphere–Thermosphere Coupling. In M. A. Abdu & D. Pancheva (Eds.), Aeronomy of the earth's atmosphere and ionosphere (pp. 191–201). Dordrecht: Springer Netherlands. doi: 10.1007/978-94-007-0326-1 13

Richmond, A. D., & Matsushita, S. (1975). Thermospheric response to a magnetic substorm. *Journal of Geophysical Research* (1896-1977), 80(19), 2839-2850. doi: 10.1029/JA080i019p02839

Rishbeth, H. (1972). Thermospheric winds and the F-region: A review. *Journal of Atmospheric and Terrestrial Physics*, 34(1), 1-47. doi: https://doi.org/10.1016/0021-9169(72)90003-7

Scherliess, L., & Fejer, B. G. (1997). Storm time dependence of equatorial disturbance dynamo zonal electric fields. *Journal of Geophysical Research: Space Physics*, 102(A11), 24037-24046. doi: 10.1029/97JA02165

Tesema, F., Mesquita, R., Meriwether, J., Damtie, B., Nigussie, M., Makela, J., Fisher, D., Harding, B., Yizengaw, E. & Sanders, S. (2017). New results on equatorial thermospheric winds and temperatures from Ethiopia, Africa. *Annales Geophysicae*, 35(2), 333–344. doi: 10.5194/angeo-35-333-2017

Valladares, C. E., Sheehan, R., Basu, S., Kuenzler, H., & Espinoza, J. (1996). The multi-instrumented studies of equatorial thermosphere aeronomy scintillation system: Climatology of zonal drifts. *Journal of Geophysical Research: Space Physics*, 101(A12), 26839-26850. doi: 10.1029/96JA00183

Xiong, C., Lühr, H., & Fejer, B. G. (2015). Global features of the disturbance winds during storm time deduced from CHAMP observations. *Journal of Geophysical Research: Space Physics*, 120(6), 5137-5150. doi: 10.1002/ 2015JA021302

Xiong, C., Lühr, H., & Fejer, B. G. (2016). The response of equatorial electrojet, vertical plasma drift, and thermospheric zonal wind to enhanced solar wind input. *Journal of Geophysical Research: Space Physics*, 121(6), 5653-5663. doi: 10.1002/2015JA022133

Zhang, S.-R., Erickson, P. J., Zhang, Y., Wang, W., Huang, C., Coster, A. J., Holt, J. M., Foster, J. F., Sulzer, M. & Kerr, R. (2017). Observations of ion-neutral coupling associated with strong electrodynamic disturbances during the 2015 St. Patrick's Day storm. *Journal of Geophysical Research: Space Physics*, 122(1), 1314-1337. doi: 10.1002/2016JA023307